Article:
Zheng, Qi, Bingham, Rory and Andrews, Oliver orcid.org/0000-0002-1921-475X (2023) Using Sea Level to Determine the Strength, Structure and Variability of the Cape Horn Current. Geophysical Research Letters. e2023GL105033. ISSN: 0094-8276

https://doi.org/10.1029/2023GL105033

Geophysical Research Letters

RESEARCH LETTER
10.1029/2023GL105033

Using Sea Level to Determine the Strength, Structure and Variability of the Cape Horn Current

Qi Zheng[1], **Rory Bingham**[1], **and Oliver Andrews**[1]

[1]School of Geographical Science, University of Bristol, Bristol, UK

Key Points:

- The Cape Horn Current (CHC) contributes to the overall Antarctic Circumpolar Current system's role as a conduit between ocean basins
- Observationally-based timeseries of CHC strength along its length are provided for the first time
- CHC strength ranges from 0.4 Sv at 49°S to 5.3 Sv at Cape Horn and is stable over recent decades

Supporting Information:

Supporting Information may be found in the online version of this article.

Correspondence to:

Q. Zheng,
qi.zheng@bristol.ac.uk

Citation:

Zheng, Q., Bingham, R., & Andrews, O. (2023). Using sea level to determine the strength, structure, and variability of the Cape Horn Current. *Geophysical Research Letters*, *50*, e2023GL105033. https://doi.org/10.1029/2023GL105033

Received 16 JUN 2023
Accepted 23 OCT 2023

Abstract The Cape Horn Current (CHC) is one of the components of the Antarctic Circumpolar Current system that enables it to fulfill its crucial role as a conduit between ocean basins. Despite this, to-date there have been very few measurements of CHC strength and none continuous in time or space. Here, we use a combination of ocean models, one free-running and one data-assimilating, and satellite altimetry (1993–2021) to estimate the time-dependent strength of the CHC at 10 transects along its length. We find the time-mean CHC transport increases from 0.4 ± 0.5 Sv near 49°S to 5.3 ± 2.2 Sv at Cape Horn, with peak-to-peak interannual fluctuations of 0.8–3.4 Sv. Although, theoretically, increased run-off from a wasting Patagonian Ice-field would strengthen its flow, the CHC appears quite stable over the last 29 years, with little evidence of a coherent, long-term increase or decrease in the strength of the current.

Plain Language Summary By connecting the Pacific, Atlantic and Indian Oceans, the Antarctic Circumpolar Current system plays a crucial role in shaping Earth's climate. One component of this current system is the Cape Horn Current (CHC) which flows south about 150 km off the coast of Chile, before entering the South Atlantic through Drake Passage. The CHC is especially important as it carries relatively freshwater, nutrients, marine larvae, and pollutants from the South Pacific and into the South Atlantic, home to globally-important fisheries and sensitive ecosystems. However, we still do not have a continuous record of the CHC strength and how it may be changing as Earth warms. In this study, we develop a method that uses numerical models of the ocean together with satellite observations of sea level to estimate the strength of the CHC over the last 29 years. We find the CHC increases in strength from 400 thousand $m^3\ s^{-1}$ in its early stages to more than 5 million $m^3\ s^{-1}$ as it rounds Cape Horn. From 1993 to 2021, the CHC appears quite stable, with little evidence of a long-term increase or decrease in the strength of the current.

1. Introduction

By connecting the Pacific, Atlantic and Indian Oceans, the Antarctic Circumpolar Current (ACC) system is a crucial element of the global ocean's circulation and Earth's climate system (e.g., Brady et al., 2021; J. Marshall & Speer, 2012; Rintoul, 2018; Watson et al., 2014). Relative to the other major currents, the structure of the ACC is complex, consisting of a system of discrete fronts, jets and flows that vary in strength, orientation and meridional separation (Kim & Orsi, 2014; Rintoul et al., 2001). As it is fed from waters leaking from the ACC downstream of the East Pacific Rise (Chaigneau & Pizarro, 2005), and returns these waters in a modified form to the ACC as it passes through Drake Passage (Acha et al., 2004; Garzón et al., 2016; Strub et al., 2013), the Cape Horn Current (CHC) can be considered a component of the overall ACC system (Lamy et al., 2015; Wu et al., 2019). Moreover, it is a component that acts as an inter-basin conduit, drawing relatively cold and fresh Subantarctic Surface Water from the South Pacific, and injecting it into the South Atlantic. Here it modifies the hydrodynamic and nutrient properties of the Patagonian Shelf (Antezana, 1999; Bianchi, 2005; Combes & Matano, 2018; Giussi et al., 2016; Guinder et al., 2020), one of the most productive and economically important fisheries in the Southern Hemisphere, before feeding into the Malvinas Current (Frey et al., 2021; Palma et al., 2021).

Despite these globally significant roles, there are very few published estimates of CHC strength, none continuous in time or space. South of 45°S and 100–150 km offshore, drifters show CHC surface velocities ranging from 15 to 35 cm s^{-1} (Chaigneau & Pizarro, 2005), while a global estimate of surface currents shows CHC speeds of up to 30 cm s^{-1} (Giesecke et al., 2021). Recently, Guihou et al. (2020) reported averaged CHC volume transport in the range of 0.08–0.95 Sv. However, this estimate comes from a model rather than observations. More studies have estimated velocities and transport of the CHC across the Drake Passage, suggesting speeds in the range of 5–30 cm s^{-1} and transports of 0.8–7.9 Sv (Boisvert, 1969; Koshlyakov

et al., 2011, 2012, 2013; Tarakanov & Gritsenko, 2018). However, an unambiguous identification of the CHC in the Drake Passage is challenging and these values are not necessarily representative of the CHC in its entirety.

Given the challenges of measuring the strength of the CHC directly along its length, here we develop a method that uses a combination of ocean modeling and satellite altimetry to estimate the strength of the CHC and how it is changing over time. The method implicitly assumes geostrophic balance. However, since only the surface flow can only be obtained directly from the sea level gradient, Δh (e.g., Alvera-Azcárate et al., 2009), we derive an empirical relationship between Δh and the depth-integrated volume transport as has been done, for example, for the Florida Current (Maul et al., 1985; Volkov et al., 2020). For the CHC, however, due to a dearth of additional observations, our empirical relationship is based on two numerical ocean models. In Section 2, the modeling and altimetry data and associated methods are described. Estimates of the CHC transport are provided in Section 3. Finally, a concluding discussion is given in Section 4.

2. Data and Methods

2.1. Model and Reanalysis Data

Our analysis depends on two ocean models. The first is the global, eddy-resolving, free-running ORCA0083-N06 version of the Nucleus for European Modeling of the Ocean (NEMO) ocean model run at the National Oceanography Center, Southampton. ORCA0083-N06, hereafter referred to as NEMO, has a nominal horizontal resolution of 1/12° and 75 vertical levels. The run covers the period 1958–2015 and is forced by the Drakkar Surface Forcing data set version 4.1 (Brodeau et al., 2010). For further details see Marzocchi et al. (2015). The second, Ocean Reanalysis System 5 (ORAS5), is a data-assimilating (sea surface temperature, sea-ice concentration, in-situ temperature and salinity, and sea level anomalies) version of NEMO, forced by ERA-Interim atmospheric reanalysis (Zuo et al., 2019). Ocean Reanalysis System 5 has the same number of vertical levels as NEMO, but has a lower horizontal resolution (1/4°) and covers the shorter period 1975 to 2014. From both models we use monthly mean sea surface height and velocity fields.

To characterize the CHC transport, and establish a relationship with sea level, we focus on 10 transects (Figure 1b). Each transect extends from the shelf to approximately 200 km off-shore and is orientated such that the flow is approximately normal to the section. The first transect crosses the CHC zonally at 49°S, 76°W and the tenth crosses the CHC meridionally at 57°S, 68°S. The total distance spanned by the sections is around 1,100 km giving an averaged interval between each transect of 123 km.

To determine the transport for each cell on a transect we first compute the velocity normal to the transect, with positive flow to the south (or east for transect 10), according to $U_n = u\cos(\pi/2 - \phi) - v\cos(\phi)$, where u and v are the zonal and meridional velocities at the center of the cell, respectively, and ϕ is the angle of the transect relative the equator. The transport is then obtained by multiplying the normal velocity by the area of the face through which it flows. For the zonal transects (1–3) and meridional transect (10), this is the area of the zonal or meridional face of the cell, whereas for the diagonal transects (4–9) it is the area of the diagonal cross-section through the cell. These are then summed vertically from the surface to 400 m, the maximum depth of the CHC suggested by the time-mean transport sections (Figure S1 in Supporting Information S1), excluding negative (e.g., equatorward) values, which are largely due to the equatorward-flowing side of the predominantly anti-cyclonic eddies crossing the off-shore CHC boundary, to obtain the total poleward/eastward transport at each grid point along a transect.

To calculate representative CHC transport timeseries, $T_i(t)$, for each transect $i = 1, \ldots, 10$, the depth summed transports (Figure S2 in Supporting Information S1) were further integrated between the CHC lateral boundaries (blue lines in Figure S2 in Supporting Information S1) which, for transects 1–8, correspond to the time-mean transport minima either side of the peak transport in NEMO. For transects 9 and 10, where the influence of the ACC makes determination of the CHC boundaries more difficult, we use the transect 8 limits, which correspond to inflection points in the normal surface current speed (see Figures S4i and S4j in Supporting Information S1). As the transport minima are not always as well-defined as in NEMO, we also use the NEMO limits for ORAS5. Because we also wish to have a single set of limits for computing the sea level difference timeseries, $\Delta h_i(t) = h_i^{on} - h_i^{off}$, we again use the NEMO limits, but with the boundary between the on-shore, h^{on}, and off-shore, h^{off}, sea level timeseries lying midway between the NEMO and ORAS5 time-mean transport peaks.

10.1029/2023GL105033

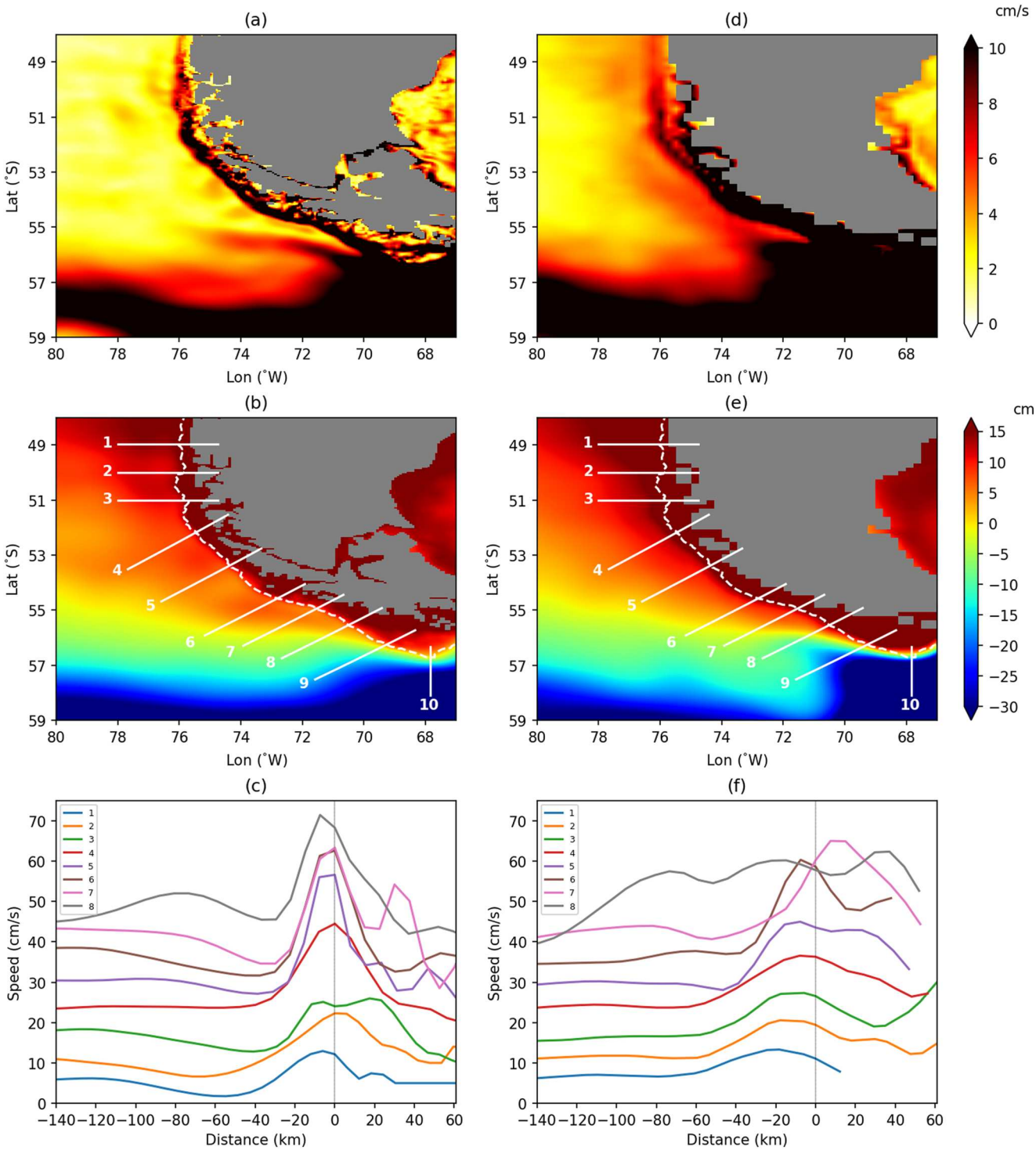

Figure 1. (a) The time-mean (1958–2015) vertical-averaged (0–400 m) current speeds in NEMO. (b) As in (a) but for the SSH. Transects are marked in white and the 500 m isobath is shown dashed. (c) The time-mean surface current speeds normal to the first eight transects, with an offset of $5n$ cm s^{-1}, where n is the transect number, added to each curve, and distance is given relative to the 500 m isobath (see Figure S4 in Supporting Information S1 for transects 9 and 10). (d-f) As in (a–c) but for the Ocean Reanalysis System 5 reanalysis averaged from 1975 to 2014.

2.2. Altimetry Data

To provide a range of transport estimates, we use three altimetry products: (a) the two-satellite (two-sat) SSH product produced and distributed by the Copernicus Climate Change Service (C3S), the stability of which makes it suitable for studying long-term change (Taburet et al., 2019); (b) the all-satellite sea level anomaly (SLA) maps (all-sat), disseminated by the Copernicus Marine Environment Monitoring Service (CMEMS), which sacrifices some stability for improved spatial resolution (Pujol et al., 2016); (c) the JPL SLA timeseries produced as part of the Multi-Mission Ocean Altimeter Data used in Research Environments (MEaSUREs) Program (Beckley et al., 2017). Since the latter two are missing the time-mean sea level, we add the CLS18 mean dynamic topography (MDT; also distributed by CMEMS). All three data sets have a horizontal resolution of $0.25° \times 0.25°$, but we interpolated onto the NEMO grid to facilitate the calculation of the SSH difference timeseries as described above. Finally, an analysis of the formal mapping errors on the CLS22 MDT and two-sat SLA's confirm that altimetry errors are small (<12%) in comparison to the sea level differences we use in this study.

3. Results

3.1. The Time-Mean Cape Horn Current

The time-mean CHC in NEMO follows the 500 m isobath poleward along the western South American Coast from 48°S to 56°S (Figure 1a). In its formative stage, the CHC is relatively weak and diffuse before emerging near 51°S as a more intense and narrowly focused current. From this point, the CHC gradually increases in strength and, to some extent, width, before merging with an un-named eastward flowing frontal current (which can also be seen in the altimetry data; see Figure S3 in Supporting Information S1) somewhere between transects 8 and 9, and then the Sub-Antarctic Front (SAF; Kim & Orsi, 2014) of the ACC between transects 9 and 10. Associated with the current is an across-slope SSH gradient, with SSH increasing toward the coast (Figure 1b).

Figure 1c (transects 1–8) and Figure S4 (all transects) in Supporting Information S1 show the time-mean surface current speed in NEMO normal to the 10 transects. Moving along each transect from the open ocean toward the coast, NEMO current speeds reach a local minimum 30–60 km from the 500 m isobath (corresponding to 0 km on the x-axis of Figure 1c) before rising to a peak within 20 km of the 500 m isobath and then declining less smoothly. Where the decline is smooth (e.g., transect 4), we can estimate the width of the CHC to be around 60 km. For transects 9–10, where the CHC merges with the SAF, the combined current widens to approximately 140 km, and becomes asymmetric with respect to the 500 m isobath, with a similar extent of 40 km toward the coast, but extending to approximately 100 km offshore (Figures S4i and S4j in Supporting Information S1). Confirming the impression from Figure 1a, peak current speeds generally increase from north to south. For the first three transects, the peak speeds are similar at 8–12 cm s^{-1} (Table 1). The peak speed increases to 24 cm s^{-1} for transect 4, and then to 28–33 cm s^{-1} for transects 5–9. Finally, for transect 10, where the CHC fully merges with the SAF, the peak velocity nearly doubles to 56 cm s^{-1}.

The CHC is also visible in ORAS5 (Figure 1d), and there is a similar marked increase in the current strength near 51°S, as seen in NEMO. However, compared to NEMO, the CHC is not as sharply defined and appears weaker to the north of 53°S, while appearing stronger to the south of this latitude. These differences are also reflected in the SSH from ORAS5 where, although the overall pattern is similar, the on-off shore gradients are not as sharp as they are in NEMO and the gradient is weaker (stronger) in the northerly (southerly) portion of the domain. There is also a marked difference, clear in the SSH maps (Figures 1b and 1e), in the path of the ACC and where it merges with the CHC. In contrast to NEMO, where the CHC merges with the SAF gradually between transects 8 and 10, in ORAS5 there is a sharp northward deflection of the SAF near 72°W such that it merges with the CHC earlier. In this respect, ORAS5 compares less favorably than NEMO with altimetry (Figure S3 in Supporting Information S1).

These differences are seen clearly in the normal surface current speeds in ORAS5 (Figure 1f). As for NEMO, peak current speeds generally increase from north to south. Although the peaks are not as clearly defined as in NEMO, for most transects, current speeds do increase from the open ocean toward the coast and reach a local maximum close to the 500 m isobath. If the core of the CHC is defined as the local maximum within 20 km of the isobath, we find similar maximum current speeds for transects 1–3 and 6–7, but lower peak speeds at transects 4–5 and 8 (Table 1). However, reflecting the more angular path taken by the ACC in ORAS5, the peak speeds for transects 9 and 10 are much greater than for NEMO.

Geophysical Research Letters

10.1029/2023GL105033

Table 1

The Strength of the Cape Horn Current and Its Relationship With Sea Level, Where $\overline{V}_{\max}$ is the Maximum Time-Mean Surface Current Speed Normal to Each Transect, $\overline{T}$ is the Time-Mean Transport, σ_T is the Unfiltered Transport Standard Deviation, $T_{max-min}$ is the Interannual Transport Range, corr(T, Δh) and β are the Correlation and Regression Coefficients Between the Transport, T, and Across-Slope Sea Level Gradient, Δh

Transect	$\overline{V}_{\max}$ (cm s^{-1})	$\overline{T}$ (Sv)	σ_T (Sv)	$T_{\max-\min}$ (Sv)	corr(T, Δh)	β (Sv cm^{-1})	$\overline{T}/\overline{\Delta h}$ (Sv cm^{-1})	Skill (%)	$\overline{\hat{T}}$ (Sv)	$\sigma_{\hat{T}}$ (Sv)	$\hat{T}_{\max-\min}$ (Sv)	Trend (Sv dec.$^{-1}$)
(1)	7.94 (8.31)	0.76 (1.00)	0.67 (0.65)	1.36 (1.68)	0.89 (0.83)	0.22 (0.23)	0.29 (0.25)	78.69 (69.59)	0.42	0.53	0.85	0.05 ± 0.08
(2)	12.29 (10.56)	1.35 (1.29)	0.76 (0.68)	1.66 (1.62)	0.90 (0.83)	0.24 (0.22)	0.26 (0.21)	80.63 (69.08)	0.98	0.62	1.05	0.00 ± 0.08
(3)	10.97 (16.86)	0.73 (1.19)	0.60 (0.59)	1.28 (1.46)	0.87 (0.92)	0.19 (0.40)	0.31 (0.31)	76.50 (84.66)	0.71	0.68	1.49	−0.04 ± 0.09
(4)	24.48 (16.56)	1.46 (1.59)	0.79 (0.65)	1.88 (1.61)	0.93 (0.88)	0.21 (0.25)	0.22 (0.20)	85.98 (77.07)	1.89	0.67	1.15	0.05 ± 0.09
(5)	31.60 (19.97)	1.26 (1.48)	0.82 (0.62)	1.85 (1.27)	0.88 (0.88)	0.18 (0.31)	0.31 (0.25)	77.69 (77.16)	1.35	0.67	1.47	−0.07 ± 0.09
(6)	32.61 (30.31)	1.53 (1.85)	0.96 (0.67)	2.28 (1.21)	0.89 (0.86)	0.17 (0.22)	0.22 (0.18)	78.42 (74.07)	2.24	0.67	1.41	−0.07 ± 0.09
(7)	28.32 (29.98)	1.20 (1.44)	0.70 (0.45)	1.27 (0.91)	0.89 (0.93)	0.16 (0.26)	0.29 (0.26)	78.39 (86.86)	1.64	0.42	0.81	−0.01 ± 0.05
(8)	31.41 (22.37)	1.68 (2.10)	0.80 (0.61)	1.65 (1.55)	0.90 (0.85)	0.18 (0.22)	0.19 (0.21)	81.87 (71.56)	2.46	0.53	1.06	0.05 ± 0.06
(9)	32.84 (45.31)	3.50 (7.10)	1.54 (2.78)	3.56 (7.65)	0.94 (0.99)	0.33 (0.42)	0.30 (0.35)	89.25 (97.83)	4.12	1.29	2.30	−0.10 ± 0.16
(10)	56.27 (98.33)	6.71 (17.92)	3.10 (4.71)	7.09 (9.80)	0.99 (0.99)	0.53 (0.67)	0.48 (0.62)	97.20 (98.68)	5.31	2.19	3.38	−0.19 ± 0.29
Mean (1 − 8)	22.45 (19.37)	1.25 (1.49)	0.76 (0.62)	1.65 (1.41)	0.89 (0.87)	0.19 (0.26)	0.26 (0.23)	79.77 (76.26)	1.46	0.60	1.16	

Note. Skill measures the agreement between the original and reconstructed transport timeseries. Values are shown for NEMO and ORAS5 (in parenthesis). $\overline{\hat{T}}$, $\sigma_{\hat{T}}$, and $\hat{T}_{\max-\min}$ refer to corresponding properties of the altimetry-based CHC reconstructions (with values the mean of the three individual altimetry products). Finally, CHC linear trends over 1993–2021 based on the two-sat altimetry product, with 95% confidence intervals, are reported.

3.2. Cape Horn Current Transports

Unlike the peak surface velocity, NEMO's time-mean CHC transport—calculated from CHC transport timeseries, $T_i(t)$ (Figure S5 in Supporting Information S1)—remains relatively constant between transects 1–8, with a minimum of 0.73 Sv at transect 3, a maximum of 1.68 Sv at transect 8 and a mean transport of 1.25 Sv across the eight transects (Table 1). The transport fluctuations are also of a similar magnitude, with a mean standard deviation (s.d.) of 0.76 Sv and, for interannual variability, a mean peak-to-peak range of 1.65 Sv. Reflecting the merging of the CHC with the SAF as Cape Horn is approached, for transect 9, the transport increases to 3.5 ± 1.5 Sv and then to 6.7 ± 3.1 Sv for transect 10, with peak-to-peak interannual fluctuations of 3.6 and 7.1 Sv, respectively.

For transects 1–8, the CHC time-mean transports in ORAS5 are slightly higher than those in NEMO, ranging from 1.0 to 1.3 Sv for transects 1–3, to 1.4–2.1 Sv for transects 4–8 (Table 1). However, the variability at all transects, as reflected in the standard deviations of the unfiltered monthly mean timeseries and the $T_{\max-\min}$ ranges of the filtered interannual timeseries (except transects 1 and 3), is weaker. For transects 9 and 10, where the CHC is joined by the SAF, the ORAS5 mean volume transport is 7.1 and 17.9 Sv, around two and three times the NEMO transports, respectively.

3.3. Relationship With Sea Level

The close relationship between T_i and Δh_i shown in Figure 2, suggests that it should be possible to use the latter to calculate the former. Table 1 confirms this to be the case. For transects 1–8, regression coefficients between T_i and Δh_i (unfiltered) range from 0.16 to 0.24 Sv cm^{-1}, with a mean of 0.19 Sv cm^{-1}, in NEMO, and from 0.22 to 0.40 Sv cm^{-1}, with a mean of 0.26 Sv cm^{-1}, in ORAS5. The higher ORAS5 values reflect weaker sea level gradients in the lower resolution model. Multiplying Δh_i by the regression coefficients yields a set of reconstructed transport timeseries, $\hat{T}_i$. For transects 1–8, the skill of these transport reconstructions (defined as the variance in the original unfiltered transport timeseries accounted for by the reconstruction) ranges from 77% (3) to 86% (4) for NEMO and 69% (2) to 87% (7) for ORAS5, with mean values of 80% and 76% for NEMO and ORAS5 (Table 1).

Of course, regression coefficients and skill scores only refer to the time-variable component of the timeseries. It is clear from Figure 2 (and Figures S6 and S7 in Supporting Information S1), however, that T_i and $\hat{T}_i$ also agree in terms of their mean values, showing the relationship implied by the regression coefficients also holds for the mean part of the fields. This is confirmed by the close agreement between the regression coefficients and $\overline{T_i}/\overline{\Delta h_i}$, the ratio of the mean transport and the mean SSH difference for each transect (Table 1). This is as expected given the two quantities are related through geostrophy.

Sea level can also be used to reconstruct transport timeseries at transects 9 and 10 where the CHC gains in strength by merging with the northern branch of the SAF. This is true for both models despite the ORAS5 transport being stronger than in NEMO, especially for transect 10 (for the reasons discussed above). For transect 9, the regression coefficients are 0.33 and 0.42 Sv cm^{-1} for NEMO and ORAS5, respectively, somewhat larger than for transects 1–8 and the skills are 89% (NEMO) and 98% (ORAS5). For transect 10, the regression coefficients increase still further to 0.53 (NEMO) and 0.67 (ORAS5) Sv cm^{-1}. Here the skill scores are the highest of all the sections, with near-perfect values of 97% (NEMO) and 99% (ORAS5).

3.4. Reconstructed Transports From Altimetry

The strong relationship between T_i and Δh_i seen in the models suggests that we can derive the actual CHC transport from observed SSH. To do this we compute Δh_i using three altimetry products and scale these timeseries by the mean of NEMO and ORAS5 regression coefficients at each transect (Figure 3). For all transects, the reconstructed volume transports, $\hat{T}_i$, from all three products are in close agreement, with the time-mean transports, $\overline{\hat{T}_i}$, over period of 1993–2021 (computed from the three individual transport estimates) increasing from 0.42 to 0.98 Sv at transects 1–3, to 1.35–2.46 Sv at transects 4–8, and finally to 4.12 (5.31) Sv at transect 9 (10) (Table 1). Likewise, the variability of the CHC is similar for each altimetry product, with mean standard deviations of 0.42–0.68 Sv at transects 1–8, increasing to 1.29 (2.19) Sv at transect 9 (10), and $\hat{T}_{\max-\min}$ ranges of 0.81–1.49 Sv at transects 1–8, increasing to 2.30 and 3.38 Sv at transects 9 and 10, respectively.

Focusing on the two-sat product, whose stability makes it most suited to detecting long-term climate signals (Taburet et al., 2019), there does not appear to be a consistent decline or increase in the strength of the CHC over

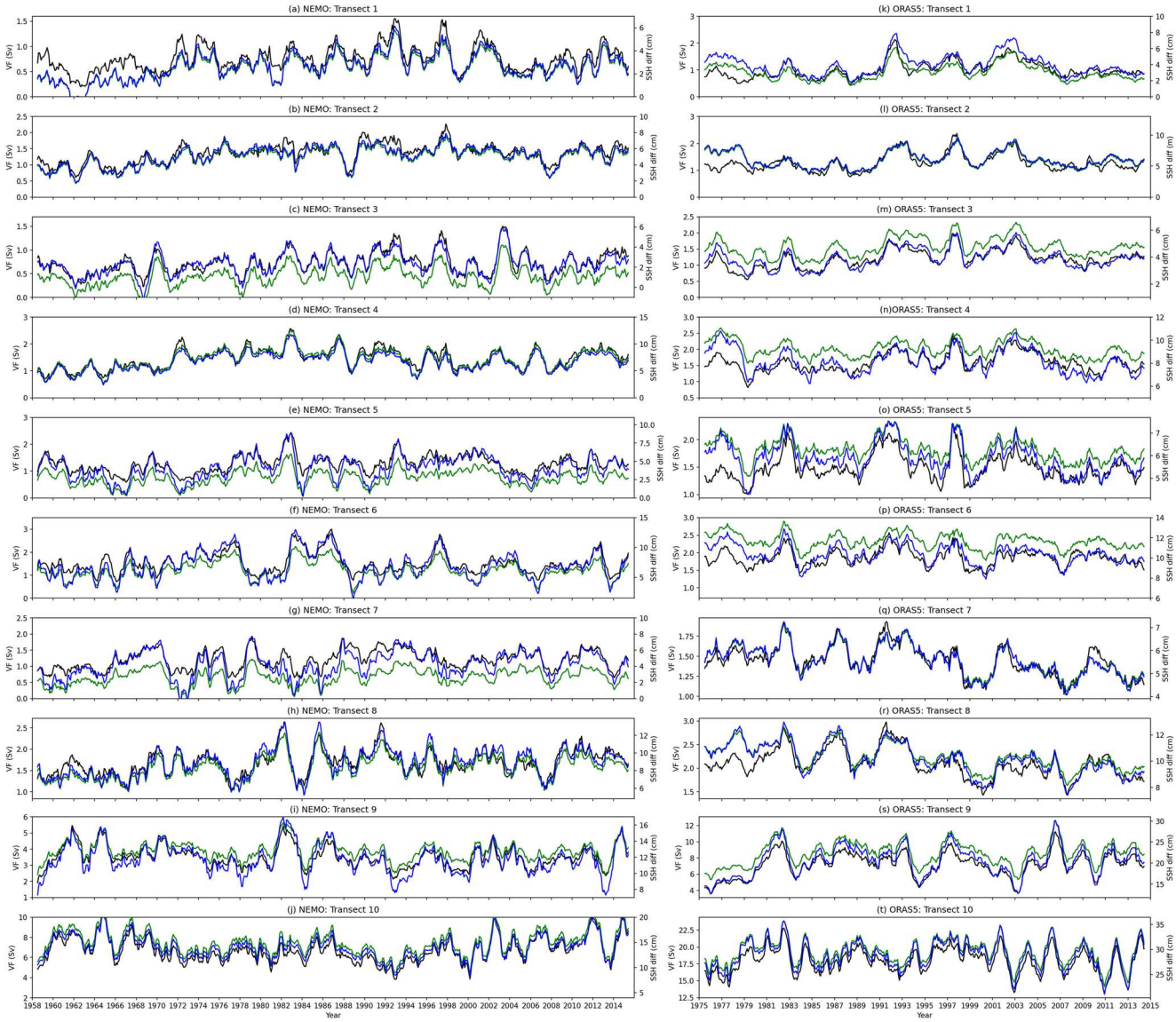

Figure 2. (a–j) The Cape Horn Current transport in NEMO at the 10 transects shown in Figure 1b (black). Also shown are the sea level gradient timeseries (blue) and reconstructed transport timeseries (green). (k–t) As for (a–j) but for Ocean Reanalysis System 5. A 1-year low-pass filter has been applied to all timeseries. Corresponding unfiltered timeseries are shown in Figures S6 and S7 in Supporting Information S1.

the altimetry period (1993–2021) (Table 1). Four transects (1, 2, 4, 8) show a weak increase in strength and the rest show a weak decrease. However, none of the trends are significantly different from zero at the 95% level. While a similar picture of a stable CHC emerges from the all-sat product, the JPL reconstruction tells a somewhat different story. In this case, all transects show a decline in CHC strength, with this decline being significantly different from zero at six transects. The largest decline of 0.21 Sv decade^{-1} (approximately 6% of the mean strength) is found at transect 9. In contrast, according to the all-sat and two-sat products, the strongest trend of −0.19 Sv decade^{-1} is found at transect 10, but this is not statistically different from zero at the 95% level (Table S1 in Supporting Information S1). Therefore, the declining trends seen in the JPL product cannot be considered robust and the evidence points toward a stable CHC over the altimetry period.

4. Concluding Discussion

In conclusion, two ocean models, one free-running and one data-assimilating, despite some differences in their representation of the CHC, both show a strong relationship between the strength of the CHC and the SSH gradient

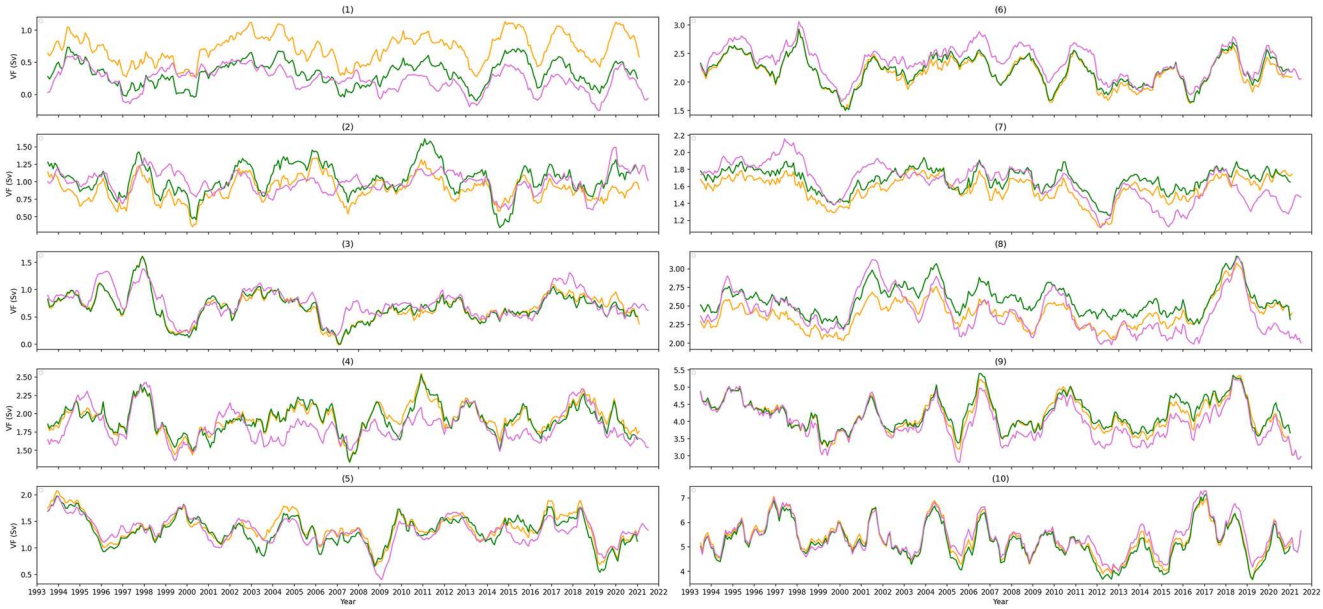

Figure 3. Timeseries of Cape Horn Current transport at the 10 transects shown in Figure 1b using the two-sat (orange), all-sat (green), and JPL (pink) sea level products. A 1-year low-pass filter has been applied to all timeseries.

across the current. This relationship holds over the entire length of the current, including where it merges with the SAF in Drake Passage. Based on this relationship, we derive the first CHC timeseries, finding the time-mean CHC transport increases from 0.4 Sv near its inception at 49°S to 5.3 Sv as it rounds Cape Horn. This latter value agrees quite closely with the mean (4.36 Sv) of three estimates of the CHC transport in Drake Passage obtained by Koshlyakov et al. (2011); Koshlyakov et al. (2012, 2013) over three consecutive cruises. Our altimetry-based estimates of the CHC are stronger than the (0.46–0.95 Sv) reported by Guihou et al. (2020). However, their estimate was based on a model rather than observations and excluded transport below 200 m, which is not negligible (Figure S1 in Supporting Information S1).

Although the agreement between the NEMO (1/12 of a degree) and ORAS5 ($\frac{1}{4}$ of a degree) ocean models gives us some confidence that the latter resolution, which is also the resolution of the altimetry products, is sufficient to resolve most, if not all, of the CHC transport, we cannot rule out an additional component of the flow for which even the resolution of NEMO is too coarse to capture. This issue should be investigated in future studies.

Given that El Niño-Southern Oscillation (ENSO) events generate coastally-trapped waves that propagate as SSH anomalies down the Pacific coast of South America (Strub & James, 2002), one might expect ENSO to impact the strength of the CHC. Inline with this expectation, for the strong 1997–1998 El Niño both models show elevated transport at transects 1–4 (Figure S5 in Supporting Information S1). However, this only occurs for isolated months and so leaves little trace at interannual timescales (Figure 2). Moreover, there is no obvious consistent pattern for across ENSO events. Nor does there seem to be a clear relationship with the Southern Annular Mode (SAM). This is in contrast to (Guihou et al., 2020) who reported that the negative phase of the SAM strengthened meridional winds and thereby the CHC. However, this may be because they focused on just the upper 200 m which is more strongly influenced by the wind. As for the trend, it is likely the interannual variability arises through a combination of mechanisms and drivers, and ENSO-SAM interactions (R. L. Fogt & Bromwich, 2006; R. Fogt et al., 2011), the relative contributions of which likely vary with latitude.

Although a full examination of the dynamics of the CHC is beyond the scope of this study, the across-slope SSH gradient is, in part, due to the relative freshness of the coastal water resulting from continental run-off (Acha et al., 2004; Dávila et al., 2002; Thiel et al., 2007). It might therefore be expected that the CHC may increase in strength as global warming increases melting of the Patagonian ice-field (Bravo et al., 2021). However, over the altimetry period, the CHC is stable, with no transects showing a statistically significant (at the 95% level) trend across at least two of the altimetry products. The JPL product suggests a more coherent pattern of CHC slowdown, but this should be treated with caution given it is not replicated in the other two products. Of course, the naive

picture painted above may be confounded by other factors such as changes in coastal precipitation (Almazroui et al., 2021) or wind forcing (Montini et al., 2019), both of which could be related to long term changes in the SAM (Gillett et al., 2006; G. J. Marshall, 2003), or other atmospheric changes. Certainly, more work and a longer observational record are required to fully elucidate the consequences of climate change on the CHC.

Data Availability Statement

Although the NEMO model output is not publicly available in its entirety, necessary subsets of the NEMO (and ORAS5) fields used in this research are available through the Zenodo Data Repository (Zheng et al., 2023). The ORAS5 data is available in Copernicus Climate Change Service (2021). The two-sat and all-sat altimetry data sets can be accessed in Copernicus Climate Change Service (2018) and in E.U. Copernicus Marine Service Information (2022), respectively. The JPL altimetry data can be found in Fournier et al. (2022). Figures were made with Matplotlib version 3.4.3 (Hunter, 2007). For review, the data derived and used in this research can be obtained in Zheng et al. (2023).

Acknowledgments
We would like to thank Dr. Andrew Coward of the National Oceanography Centre, UK for providing the NEMO data used in this study, and Dr. Chris Wilson and two anonymous reviewers for comments that help improve the manuscript.

References

Acha, E. M., Mianzan, H. W., Guerrero, R. A., Favero, M., & Bava, J. (2004). Marine fronts at the continental shelves of austral south America: Physical and ecological processes. *Journal of Marine Systems*, *44*(1), 83–105. https://doi.org/10.1016/j.jmarsys.2003.09.005

Almazroui, M., Ashfaq, M., Islam, M. N., Rashid, I. U., Kamil, S., Abid, M. A., et al. (2021). Assessment of CMIP6 performance and projected temperature and precipitation changes over south America. *Earth Systems and Environment*, *5*(2), 155–183. https://doi.org/10.1007/s41748-021-00233-6

Alvera-Azcárate, A., Barth, A., & Weisberg, R. H. (2009). The surface circulation of the Caribbean Sea and the Gulf of Mexico as inferred from satellite altimetry. *Journal of Physical Oceanography*, *39*(3), 640–657. https://doi.org/10.1175/2008jpo3765.1

Antezana, T. (1999). Hydrographic features of Magellan and Fuegian inland passages and adjacent Subantarctic waters. *Scientia Marina*, *63*(S1), 23–34. https://doi.org/10.3989/scimar.1999.63s123

Beckley, B. D., Callahan, P. S., Hancock, D. W., III, Mitchum, G. T., & Ray, R. D. (2017). On the "Cal-Mode" correction to TOPEX satellite altimetry and its effect on the global mean sea level time series. *Journal of Geophysical Research: Oceans*, *122*(11), 8371–8384. https://doi.org/10.1002/2017jc013090

Bianchi, A. A., Bianucci, L., Piola, A. R., Pino, D. R., Schloss, I., Poisson, A., & Balestrini, C. F. (2005). Vertical stratification and air-sea CO_2 fluxes in the Patagonian shelf. *Journal of Geophysical Research*, *110*(C7), C07003. https://doi.org/10.1029/2004jc002488

Boisvert, W. E. (1969). *Major currents off the west coasts of north and south America (technical report)*. Naval Oceanographic Office NSTL Station MS.

Brady, R. X., Maltrud, M. E., Wolfram, P. J., Drake, H. F., & Lovenduski, N. S. (2021). The influence of ocean topography on the upwelling of carbon in the southern ocean. *Geophysical Research Letters*, *48*(19), e2021GL095088. https://doi.org/10.1029/2021gl095088

Bravo, C., Bozkurt, D., Ross, A. N., & Quincey, D. J. (2021). Projected increases in surface melt and ice loss for the Northern and Southern Patagonian icefields. *Scientific Reports*, *11*(1), 16847. https://doi.org/10.1038/s41598-021-95725-w

Brodeau, L., Barnier, B., Treguier, A.-M., Penduff, T., & Gulev, S. (2010). An ERA40-based atmospheric forcing for global ocean circulation models. *Ocean Modelling*, *31*(3), 88–104. https://doi.org/10.1016/j.ocemod.2009.10.005

Chaigneau, A., & Pizarro, O. (2005). Surface circulation and fronts of the South Pacific Ocean, east of 120°W. *Geophysical Research Letters*, *32*(8), L08605. https://doi.org/10.1029/2004gl022070

Combes, V., & Matano, R. P. (2018). The Patagonian shelf circulation: Drivers and variability. *Progress in Oceanography*, *167*, 24–43. https://doi.org/10.1016/j.pocean.2018.07.003

Copernicus Climate Change Service, C. D. S. (2018). Sea level gridded data from satellite observations for the global ocean from 1993 to present [Dataset]. Advances in Contraceptive Delivery Systems. https://doi.org/10.24381/cds.4c328c78

Copernicus Climate Change Service, C. D. S. (2021). ORAS5 global ocean reanalysis monthly data from 1958 to present [Dataset]. Copernicus Climate Change Service (C3S) Climate Data Store (CDS). https://doi.org/10.24381/cds.67e8eeb7

Dávila, P. M., Figueroa, D., & Müller, E. (2002). Freshwater input into the coastal ocean and its relation with the salinity distribution off austral Chile (35–55 s). *Continental Shelf Research*, *22*(3), 521–534. https://doi.org/10.1016/s0278-4343(01)00072-3

E. U. Copernicus Marine Service Information, M. D. S. (2022). Global Ocean gridded L4 sea surface heights and derived variables reprocessed 1993 ongoing [Dataset]. Copernicus. https://doi.org/10.48670/moi-00148

Fogt, R., Bromwich, D., & Hines, K. (2011). Understanding the SAM influence on the south pacific ENSO teleconnection. *Climate Dynamics*, *36*(7–8), 1555–1576. https://doi.org/10.1007/s00382-010-0905-0

Fogt, R. L., & Bromwich, D. H. (2006). Decadal variability of the ENSO teleconnection to the high-latitude south pacific governed by coupling with the southern annular mode. *Journal of Climate*, *19*(6), 979–997. https://doi.org/10.1175/jcli3671.1

Fournier, S., Willis, K. J., Killett, E., Qu, Z., & Zlotnicki, V. (2022). SEA_SURFACE_HEIGHT_ALT_GRIDS_L4_2SATS_5DAY_6THDE-G_V_JPL2205. Ver. 2205 [Dataset]. PO.DAAC, CA, USA. https://doi.org/10.5067/SLREF-CDRV3

Frey, D. I., Piola, A. R., Krechik, V. A., Fofanov, D. V., Morozov, E. G., Silvestrova, K. P., et al. (2021). Direct measurements of the Malvinas current velocity structure. *Journal of Geophysical Research: Oceans*, *126*(4), e2020JC016727. https://doi.org/10.1029/2020jc016727

Garzón, J. E. C., Martínez, A. M., Barrera, F., Pfaff, F., Koch, B. P., Freije, R. H., et al. (2016). The Pacific-Atlantic connection: Biogeochemical signals in the southern end of the argentine shelf. *Journal of Marine Systems*, *163*, 95–101. https://doi.org/10.1016/j.jmarsys.2016.07.008

Giesecke, R., Martín, J., Piñones, A., Höfer, J., Garcés-Vargas, J., Flores-Melo, X., et al. (2021). General hydrography of the Beagle Channel, a subantarctic interoceanic passage at the southern tip of South America. *Frontiers in Marine*, *8*, 621822. https://doi.org/10.3389/fmars.2021.621822

Gillett, N. P., Kell, T. D., & Jones, P. D. (2006). Regional climate impacts of the southern annular mode. *Geophysical Research Letters*, *33*(23), L23704. https://doi.org/10.1029/2006gl027721

Giussi, A. R., Gorini, F. L., Di Marco, E. J., Zavatteri, A., & Marí, N. (2016). *Biology and fishery of the Southern hake (Merluccius australis) in the southwest Atlantic Ocean*. Revista de Investigacion y Desarrollo Pesquero.

Guihou, K., Piola, A. R., Palma, E. D., & Chidichimo, M. P. (2020). Dynamical connections between large marine ecosystems of austral South America based on numerical simulations. *Ocean Science*, *16*(2), 271–290. https://doi.org/10.5194/os-16-271-2020

Guinder, V. A., Malits, A., Ferronato, C., Krock, B., Garzón-Cardona, J., & Martínez, A. (2020). Microbial plankton configuration in the epipelagic realm from the beagle channel to the Burdwood bank, a marine protected area in Sub-Antarctic waters. *PLoS One*, *15*(5), e0233156. https://doi.org/10.1371/journal.pone.0233156

Hunter, J. D. (2007). Matplotlib: A 2D graphics environment [Software]. Computing in Science & Engineering, *9*(3), 90–95. https://doi.org/10.1109/MCSE.2007.55

Kim, Y. S., & Orsi, A. H. (2014). On the variability of Antarctic circumpolar current fronts inferred from 1992–2011 altimetry. *Journal of Physical Oceanography*, *44*(12), 3054–3071. https://doi.org/10.1175/jpo-d-13-0217.1

Koshlyakov, M. N., Gladyshev, S. V., Tarakanov, R. Y., & Fedorov, D. A. (2011). Currents in the western drake passage according to the observations in January of 2010. *Oceanology*, *51*(2), 187–198. https://doi.org/10.1134/s000143701102007x

Koshlyakov, M. N., Gladyshev, S. V., Tarakanov, R. Y., & Fedorov, D. A. (2012). Currents in the drake passage based on the observations in November of 2010. *Oceanology*, *52*(3), 299–308. https://doi.org/10.1134/s000143701203006x

Koshlyakov, M. N., Gladyshev, S. V., Tarakanov, R. Y., & Fedorov, D. A. (2013). Currents in the drake passage by the observations in October–November of 2011. *Oceanology*, *53*(1), 1–12. https://doi.org/10.1134/s0001437013010062

Lamy, F., Arz, H. W., Kilian, R., Lange, C. B., Lembke-Jene, L., Wengler, M., et al. (2015). Glacial reduction and millennial-scale variations in drake passage throughflow. *Proceedings of the National Academy of Sciences of the United States of America*, *112*(44), 13496–13501. https://doi.org/10.1073/pnas.1509203112

Marshall, G. J. (2003). Trends in the southern annular mode from observations and reanalyses. *Journal of Climate*, *16*(24), 4134–4143. https://doi.org/10.1175/1520-0442(2003)016<4134:titsam>2.0.co;2

Marshall, J., & Speer, K. (2012). Closure of the meridional overturning circulation through Southern Ocean upwelling. *Nature Geoscience*, *5*(3), 171–180. https://doi.org/10.1038/ngeo1391

Marzocchi, A., Hirschi, J. J.-M., Holliday, N. P., Cunningham, S. A., Blaker, A. T., & Coward, A. C. (2015). The North Atlantic subpolar circulation in an eddy-resolving global ocean model. *Journal of Marine Systems*, *142*, 126–143. https://doi.org/10.1016/j.jmarsys.2014.10.007

Maul, G. A., Chew, F., Bushnell, M., & Mayer, D. A. (1985). Sea level variation as an indicator of Florida current volume transport: Comparisons with direct measurements. *Science*, *227*(4684), 304–307. https://doi.org/10.1126/science.227.4684.304

Montini, T. L., Jones, C., & Carvalho, L. M. V. (2019). The South American low-level jet: A new climatology, variability, and changes. *Journal of Geophysical Research*, *124*(3), 1200–1218. https://doi.org/10.1029/2018jd029634

Palma, E. D., Matano, R. P., & Combes, V. (2021). Circulation and cross-shelf exchanges in the Malvinas islands shelf region. *Progress in Oceanography*, *198*, 102666. https://doi.org/10.1016/j.pocean.2021.102666

Pujol, M.-I., Faugère, Y., Taburet, G., Dupuy, S., Pelloquin, C., Ablain, M., & Picot, N. (2016). DUACS DT2014: The new multi-mission altimeter data set reprocessed over 20 years. *Ocean Science*, *12*(5), 1067–1090. https://doi.org/10.5194/os-12-1067-2016

Rintoul, S. R. (2018). The global influence of localized dynamics in the southern ocean. *Nature*, *558*(7709), 209–218. https://doi.org/10.1038/s41586-018-0182-3

Rintoul, S. R., Hughes, C. W., & Olbers, D. (2001). Antarctic circumpolar current system. In *International geophysics* (Vol. 77, pp. 271–XXXVI). Elsevier.

Strub, P. T., Combes, V., Shillington, F. A., & Pizarro, O. (2013). Currents and processes along the eastern boundaries. *International Geophysics*, 339–384. https://doi.org/10.1016/b978-0-12-391851-2.00014-3

Strub, P. T., & James, C. (2002). The 1997–1998 oceanic el niño signal along the southeast and northeast pacific boundaries—An altimetric view. *Progress in Oceanography*, *54*(1), 439–458. https://doi.org/10.1016/s0079-6611(02)00063-0

Taburet, G., Sanchez-Roman, A., Ballarotta, M., Pujol, M.-I., Legeais, J.-F., Fournier, F., et al. (2019). DUACS DT2018: 25 years of reprocessed sea level altimetry products. *Ocean Science*, *15*(5), 1207–1224. https://doi.org/10.5194/os-15-1207-2019

Tarakanov, R. Y., & Gritsenko, A. M. (2018). Jets of the Antarctic circumpolar current in the drake passage based on hydrographic section data. *Oceanology*, *58*(4), 503–516. https://doi.org/10.1134/s0001437018040100

Thiel, M., Macaya, E., Acuña, E., Arntz, W., Bastias, H., Brokordt, K., et al. (2007). The Humboldt Current System of northern and central Chile. In *Oceanography and marine biology* (pp. 195–344). CRC Press.

Volkov, D. L., Domingues, R., Meinen, C. S., Garcia, R., Baringer, M., Goni, G., & Smith, R. H. (2020). Inferring Florida Current volume transport from satellite altimetry. *Journal of Geophysical Research: Oceans*, *125*(12), 717. https://doi.org/10.1029/2020jc016763

Watson, A. J., Meredith, M. P., & Marshall, J. (2014). The southern ocean, carbon and climate. *Philosophical Transactions of the Royal Society A*, *372*(2019), 20130057. https://doi.org/10.1098/rsta.2013.0057

Wu, S., Kuhn, G., Diekmann, B., Lembke-Jene, L., Tiedemann, R., Zheng, X., et al. (2019). Surface sediment characteristics related to provenance and ocean circulation in the drake passage sector of the southern ocean. *Deep-Sea Research Part A: Oceanographic Research Papers I*, *154*, 103135. https://doi.org/10.1016/j.dsr.2019.103135

Zheng, Q., Bingham, R., & Andrews, O. (2023). Using sea level to determine the strength, structure and variability of the Cape Horn Current [Dataset]. Zenodo. https://doi.org/10.5281/zenodo.8299628

Zuo, H., Balmaseda, M. A., Tietsche, S., Mogensen, K., & Mayer, M. (2019). The ECMWF operational ensemble reanalysis-analysis system for ocean and sea ice: A description of the system and assessment. *Ocean Science*, *15*(3), 779–808. https://doi.org/10.5194/os-15-779-2019